Thermal analysis of a water-cooled interior permanent magnet traction machine

Conference Paper · February 2013

DOI: 10.1109/ICIT.2013.6505708

2 authors, including:

Rong-Jie Wang
Stellenbosch University
132 PUBLICATIONS **2,838** CITATIONS

SEE PROFILE

Thermal Analysis of a Water-Cooled Interior Permanent Magnet Traction Machine

R-J. Wang and G. C. Heyns
Dept of Electrical and Electronic Engineering
Stellenbosch University
Matieland, 7602, South Africa
Email: rjwang@ieee.org

***Abstract*—This paper presents the thermal analysis of a water-cooled interior permanent magnet (IPM) machine. An efficient quasi-3D lumped parameter thermal model is described and then applied to a practical IPM machine. The analytical model is validated by comparing its results with those obtained using detailed two-dimensional and three-dimensional finite element thermal analysis. Relevant conclusions are drawn.**

I. Introduction

Interior permanent magnet (IPM) synchronous machines have many advantages such as high efficiency, high torque density and wide constant power speed range (CPSR), which make this type of machine an attractive candidate for traction applications. Given the safety critical nature of traction applications, the machines are usually totally enclosed with water cooling to protect them from any adverse environment [1].

From a cooling design perspective, it is important to accurately predict the temperatures of various components inside the machine at the design stage so that the temperature limitations established for the machine materials such as winding insulation and permanent magnets (PM) are complied with. Two basic analysis techniques are often used for the purpose, i.e. the lumped parameter thermal model (LPTM) and the finite element method (FEM) [2], [3].

The FEM thermal analysis can accurately compute the temperature distribution inside the machine and identify hot spots of key machine components. With three-dimension (3D) FEM, the effect of end-winding, slot insulation, contact thermal resistances can also be accounted for. However, the FEM thermal analysis, especially the 3D FEM, tends to be computationally expensive. This becomes even more so when the heat transfer boundary conditions are determined by using computational fluid dynamics (CFD) packages.

The LPTM analysis is an efficient alternative for estimating the key temperatures inside an electric machine as the analysis can be done rapidly. The resolution of a LPTM can be improved by increasing the number of thermal nodes. By including the effects of end-winding, insulation, mechanical interface and surrounding structures (bearings, end-shields etc.), a LPTM becomes effectively a quasi-3D analytical model. The LPTM can be easily incorporated into the system-level dynamic drive-cycle simulations. There have been some published research work describing LPTMs for PM machines [1], [4], [5].

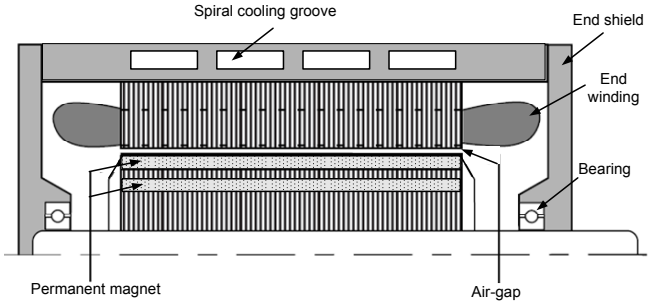

Fig. 1: The longitudinal sectional view of the IPM machine showing the mechanical layout.

TABLE I: Machine dimensions and design specifications

Parameters	Values
Rated shaft power (kW)	51
Rated shaft torque (Nm)	180
Rated speed (RPM)	2700
Rated line current (RMS) (A)	180
Rated line voltage (RMS) (V)	187
Number of stator slots	36
Number of pole-pairs	3
Stator outer diameter (mm)	240
Stator bore diameter (mm)	142
Air-gap length (mm)	0.5
Number of turns per slot	14
Stator winding layout	full-pitch/distributed
Magnet type	NdFeB 45SH

This paper presents a quasi-3D LPTM for the thermal analysis of a water-cooled IPM traction machine shown in Fig. 1. The results are then compared with those of 2D and 3D FEM analysis, which outlines both the advantages and disadvantages of each method.

II. The IPM machine under study

A. The design specifications

The basic machine dimensions and the rated specifications of the IPM traction machine under study are summarized in Table I. The machine is designed to have a CPSR of 3, which enables the machine to achieve a field weakening operation up to 8100 rpm. The main emphasis of this thermal study is on the rated condition.

978-1-4673-4568-2/13/$31.00 ©2012 IEEE

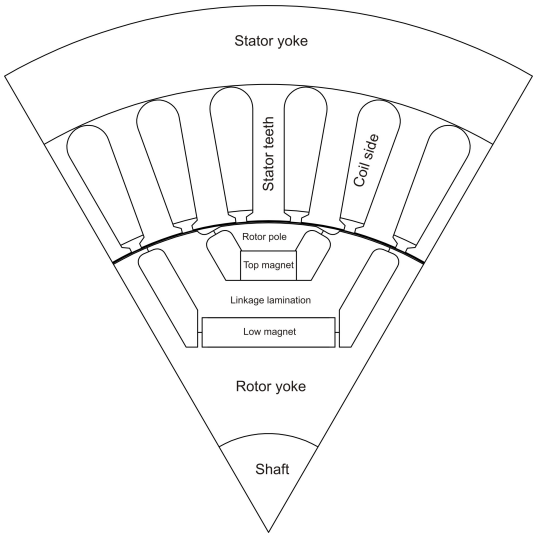

Fig. 2: Various parts of the machine, where heat losses were computed.

B. Losses calculation

The electromagnetic losses (winding copper loss, magnet Joule loss, and stator and rotor iron loss) under rated condition were calculated from 2D FE analysis. To facilitate the analytical calculation and comparison, the losses of each designated region in the 2D FE model shown in Fig. 2 are extracted from the FE losses results.

1) Stator winding copper losses: The stator winding copper losses are calculated according to $P_s = 3I_s^2 R_s$, where I_s is the rms phase current and R_s is the stator phase resistance at working temperature.

2) Stator and rotor iron losses: The iron losses computation for a stator or a rotor requires the detailed loss curves of its lamination material at different frequencies. The total iron losses of a stator or a rotor core may be expressed as:

$$P_t = P_h + P_j \tag{1}$$

where P_t is the total iron loss of the stator or the rotor, P_h is the hysteresis loss component and P_j is the Joule loss component.

The hysteresis losses are calculated by the 2D FE program using the apply loop approach as follow [6]

$$P_h = \sum_{e=1}^{\mathrm{n_{elem}}} \left\{ f \sum_{k=1}^{\mathrm{n_{loop}}} \alpha(B_k) \times V_e \right\} \tag{2}$$

where f is the fundamental frequency, $\alpha(B)$ is the coefficient of magnetic flux density determined by the frequency separation method [6], B_k is the amplitude of the k^{th} loop for each component of magnetic flux density, V_e is the size of each element, n_{loop} is the number of hysteresis loops considered and n_{elem} is the number of mesh elements of the iron part.

The Joule loss component is also determined by the 2D FE program using the frequency analysis approach [6]

TABLE II: Loss values for different regions of the machine

Machine Parts	Losses (W)
Stator yoke	115
Stator teeth	246
Rotor pole	10
Rotor yoke	13
Linkage lamination	16
Top magnets (NdFeB 45SH)	1.6
Low magnets (NdFeB 45SH)	6.3
Main winding	769
End windings	769
Rotor (wind and friction)	275

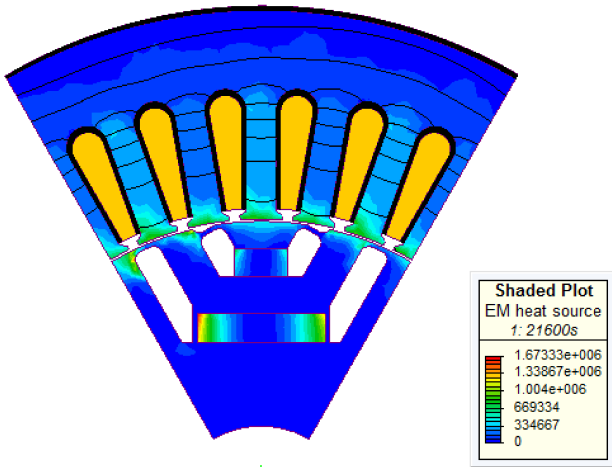

Fig. 3: Calculated loss distribution inside the machine.

$$P_j = \sum_{e=1}^{\mathrm{n_{elem}}} \left\{ \sum_{k=1}^{N} b(|B_k|, f_k) \times {f_k}^2 \right\} \times V_e \tag{3}$$

where f_k is the k^{th} order frequency, $b(|B_k|, f_k)$ is the coefficient of magnetic flux density $|B_k|$ determined by the frequency separation method at f_k [6], B_k^* is the complex conjugate of B_k, and N is the maximum frequency order. The Magnet Joule losses can be calculated using a classical approach [7] shown below:

$$P_{mj} = \sum_{e=1}^{\mathrm{n_{elem}}} \left\{ \frac{b^2}{12\ \rho_m} \cdot \left(\frac{dB}{dt} \right)^2 \right\} \times V_e \tag{4}$$

where b is the PM breadth, ρ_m is the PM material resistivity and B is the resultant magnetic flux density in an element.

3) Windage and friction losses: The mechanical windage and friction loss forms part of the total rotor losses and are estimated analytically by using the following relation [8]:

$$P_{wf} = 2D_r^3 L_r n^3 \times 10^{-6} + k_{fb} G_r n \times 10^{-3} \tag{5}$$

where D_r is the outside diameter of the rotor, L_r is the axial length of the rotor core, n is the rotation speed, k_{fb} is the rotational loss constant, and G_r is the mass of the rotor.

Table II shows the calculated losses of different regions defined in Fig. 2 for rated operating condition. Fig. 3 depicts the calculated loss distribution inside the machine.

TABLE III: Thermal properties of the materials in a PM motor

Material type	Density [kg/m^3]	Heat conductivity [W/m.K]	Specific heat [J/kg.K]
Steel lamination	7600	32	460
Aluminum (housing)	2705	230	896
Magnet (NdFeB)	7500	6.75	460
Steel C:1% (shaft)	7800	51	420
Copper (winding)	8900	395	385
Air (40°C)	1.09	0.0265	1014
Normex slot liner	950	0.143	1170
Water (20°C)	998	0.58	4190
Bearing steel	7800	30	460
Epoxy resin	1400	0.21	1700
Polyimide (wire)	1430	0.35	1130

TABLE IV: Definition of thermal resistances

Symbol	Definition
R_1	Convection resistance from frame to water
R_2	Conduction resistance from stator yoke to frame
R_3	Conduction resistance from stator teeth to stator yoke
R_4	Conduction resistance from main winding to stator teeth
R_5	Conduction resistance from end-winding to main-winding
R_6	Convection resistance from end-winding to end space
R_7	Convection resistance from stator teeth to air-gap
R_8	Convection resistance from air-gap to rotor pole
R_9	Conduction resistance from rotor pole to top magnet
R_{10}	Conduction resistance from top magnet to link lamination
R_{11}	Conduction resistance from link lamination to low magnet
R_{12}	Conduction resistance from low magnet to yoke
R_{13}	Conduction resistance from yoke to shaft
R_{14}	Conduction resistance from shaft to bearing
R_{15}	Conduction resistance from bearing to end shields
R_{16}	Conduction resistance from end shields to frame
R_{17}	Convection resistance from end space to end shields
R_{18}	Convection resistance from end space to frame
R_{19}	Convection resistance from air-gap to rotor link lamination
R_{20}	Convection resistance from air-gap to rotor yoke
R_{21}	Radiation resistance from end-winding to end shields

III. Quasi-3D Analytical thermal model

The LPTMs are commonly used for analytical thermal analysis. For steady-state analysis, a LPTM is made up of only thermal nodes, thermal resistances (*conduction*, *convection* and *radiation*) and heat sources while for transient analysis, it also includes thermal capacitances. The calculation of thermal resistances and capacitances requires the properties of materials. Table III gives the thermal properties of materials applied to the thermal analysis of the IPM machine.

A. 2D analytical model

Fig. 4 shows the configuration of the complete LPTM for the IPM machine, which consists of a network with 16 nodes representing various key components of the machine. The definition of each thermal resistance is given in Table IV. To simplify the analysis, it is assumed that heat flows radially in the cross-section plane of the machine. Hence, the active section of the machine can be basically represented by a 2D LPTM. The thermal resistance of a cylindrical section R_c with an angular span θ can be calculated by [9]:

$$R_c = \frac{\ln(r_o) - \ln(r_i)}{kL\theta} \tag{6}$$

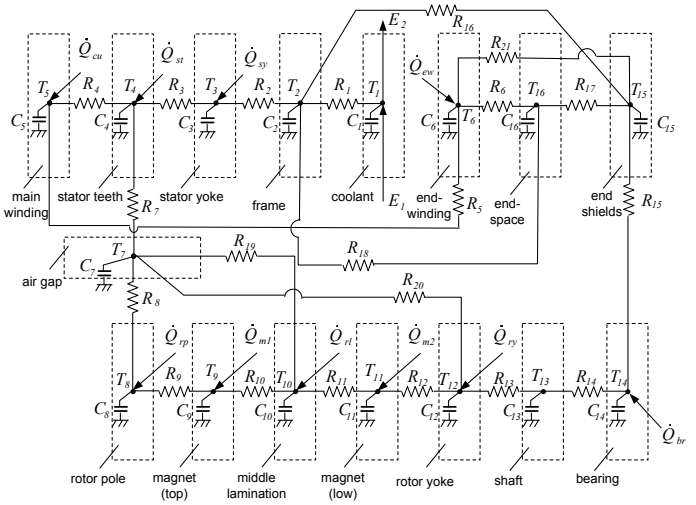

Fig. 4: The quasi-3D lumped parameter thermal network of the machine.

where L is the axial length, r_i and r_o are the inner and outer radius of the cylindrical section respectively.

Since the winding temperature is of critical importance in the thermal analysis of an electric machine, an accurate representation of the coil sides and stator slots in the thermal model is essential. Several useful modeling techniques have been developed to transform a generic stator slot area into a rectangular shape [10] and to derive a single-nodal expression of the stator tooth [11].

1) Heat transfer of cooling channels: The heat transfer coefficient of the turbulent flow in the spiral housing water jacket may be calculated according to [12]:

$$h_c = \frac{k_w}{D_h} \times \mathrm{Re}^{0.8} \times \mathrm{Pr}^{0.35} \tag{7}$$

$$\mathrm{Re} = \frac{\rho_w v D_h}{\mu_w}; \quad D_h = \frac{4\mathbf{A}}{\wp} \tag{8}$$

where Re is the Reynolds number, ρ_w is the density of water, v is the water flow velocity, k_w is water thermal conductivity, D_h is the hydraulic diameter, Pr is the Prandtl number, $\wp$ is the periphery length of the water channel, $\mathbf{A}$ is the cross section area of the channel, and μ_w is the dynamic viscosity of water.

2) Heat transfer across the air-gap: The convective heat transfer between the stator and rotor can be calculated by using the following empirical relations [13]:

$$h_{ag} = \frac{\mathrm{Nu}\ k_a}{2\ l_g} \tag{9}$$

where k_a is the thermal conductivity of air, l_g is the air-gap length and Nu is the Nusselt number defined by:

$$Nu = \begin{cases} 0.409\ Ta^{0.241} - 137\ Ta^{-\frac{3}{4}} & \text{(turbulent)} \\ 2 & \text{(laminar)} \end{cases} \tag{10}$$

where

$$Ta = \frac{\omega_m^2\ r_{ag}\ l_g^3}{\nu_a^2} \tag{11}$$

Taylor number T_a is a function of mechanical angular speed ω_m, air-gap radius r_{ag} and the kinematic viscosity of air ν_a and is used to determine the flow condition.

3) Mechanical interfaces: The thermal contact resistance of any mechanical interface depends on many factors such as material hardness, interface pressure and surface conditions. When two solid surfaces are in contact, there exists an imperfect surface junction, which creates a temperature gradient between the two surfaces. The effects of the contact resistance between stator lamination and water-cooled frame has been experimentally investigated in [14].

The accuracy of the thermal performance prediction is quite sensitive to the thermal contact resistances such as those of stator lamination to machine frame, slot lining to stator teeth and magnets to rotor lamination. In this paper, an interface gap of 0.03 mm has been assumed for all the mechanical surface junctions. The thermal contact resistance is calculated by using $R_{if} = l_{if}/(k_a A_{if})$, where l_{if} is the interference gap and A_{if} is the interference area.

B. Heat transfer in axial direction

So far the LPTM only considered the radial heat transfer, which may be acceptable for the active section of the machine. This is because the axial heat flow in the machine's active section is limited by inter-lamination gaps and insulation layers. However, there are heat flows in axial direction that cannot be neglected, e.g. heat flow from end-winding to main winding, from end-winding to end-space air, and heat flow along the shaft. Leaving out these axial heat flows in the LPTM may cause significant error in the analysis. Usually the end-winding area has a higher average temperature than that of the main winding. To account for the heat loss and temperature difference of the end-winding, an end-winding node was defined on the LPTM.

1) Heat transfer between end-winding and end-shields: Heat flow from the end winding to the end space by convection may be calculated using the following empirical relation [15]

$$h_{ew} = 6.5 + 5.25^{0.65} v_r^{0.6} \tag{12}$$

where v_r is the rotor peripheral speed (m/s). The radiation resistance between the end-winding and end-shield surfaces, A_1 and A_2, with respective absolute temperatures, T_1 and T_2, is calculated by:

$$R_r = \frac{\frac{1-\epsilon_1}{\epsilon_1 A_1} + \frac{1}{A_1 F_{12}} + \frac{1-\epsilon_2}{\epsilon_2 A_2}}{\sigma (T_1 + T_2)(T_1^2 + T_2^2)} \tag{13}$$

where ϵ_1 and ϵ_2 are surface emissivities, F_{12} is the form factor for relative orientation of two surfaces, and σ is *Stefan-Boltzmann* constant.

2) Shaft thermal resistance: The thermal resistance of the shaft can be calculated as

$$R_{sh} = \frac{l_{sh}}{\pi {r_{sh}}^2 k_{sh}} \tag{14}$$

where r_{sh}, l_{sh} and k_{sh} are the radius, the axial length, and the thermal conductivity of the shaft respectively.

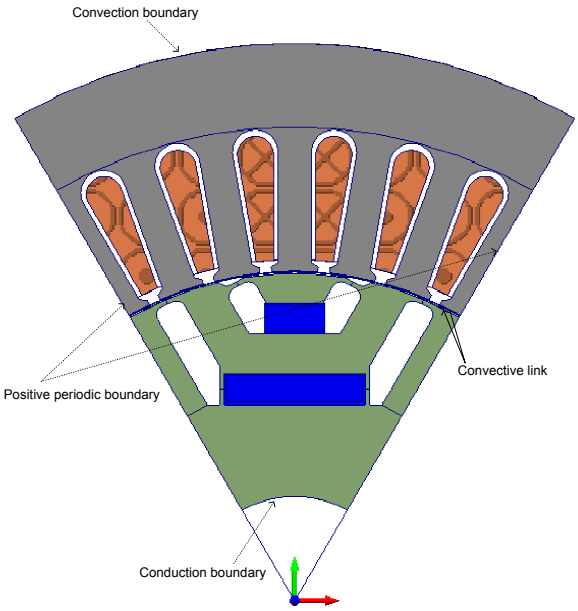

Fig. 5: 2D FE thermal model of the IPM machine.

C. Conservation of energy

If each component of a machine is represented by a control volume, based on the principle of conservation of energy, the rate of temperature change of each control volume under transient conditions can be expressed as follows:

$$\frac{\Delta T}{\Delta t} = \frac{1}{C}(\Delta \dot{Q}_{in} - \Delta \dot{Q}_{out} + \dot{m}_{in} i_{in} - \dot{m}_{out} i_{out}) \tag{15}$$

where $\dot{m}$ is the mass flow rate, i is the enthalpy and C is the thermal capacitance of a control volume, which is the product of the mass and the heat capacity of the material in the control volume. For steady-state, $\Delta T/\Delta t = 0$ thus

$$\Delta \dot{Q}_{in} - \Delta \dot{Q}_{out} + \dot{m}_{in} i_{in} - \dot{m}_{out} i_{out} = 0 \tag{16}$$

If the above relation is applied to each control volume, a set of equations with temperature of each volume being the only unknowns are formulated, which can be solved using an iterative approach such as *Gauss-Seidel iteration*.

IV. FEM THERMAL CALCULATION

A. 2D FEM analysis

The 2D FE thermal model of the IPM machine is shown in Fig. 5. The commercial 2D FE thermal package *ThermNet* has been used for the analysis. By taking the advantage of the symmetrical geometry, it is only necessary to model 1/6th of the whole machine by applying the periodic boundary condition to the left and right boundaries. The cooling effect due to the water channel is accounted by assigning a convection boundary condition to the top boundary while the heat dissipation through the shaft is represented by a virtual convection boundary condition.

To more accurately account for the thermal resistance of the stator slot lining, impregnation and insulation, an artificial

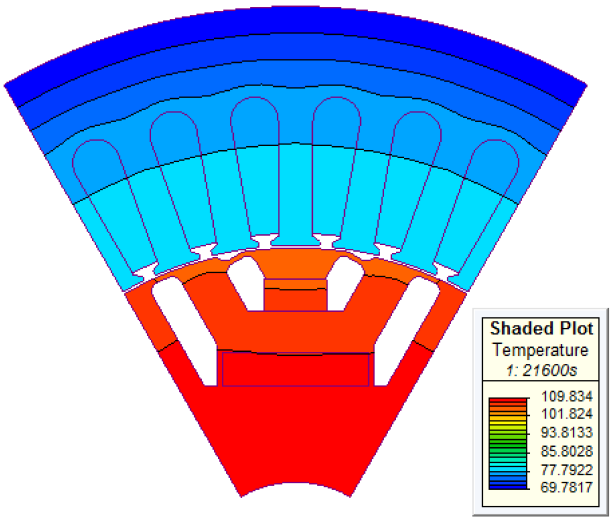

Fig. 6: 2D temperature distribution in the IPM machine without taking into account the stator slot lining, impregnation and insulation (coolant temperature 50°C).

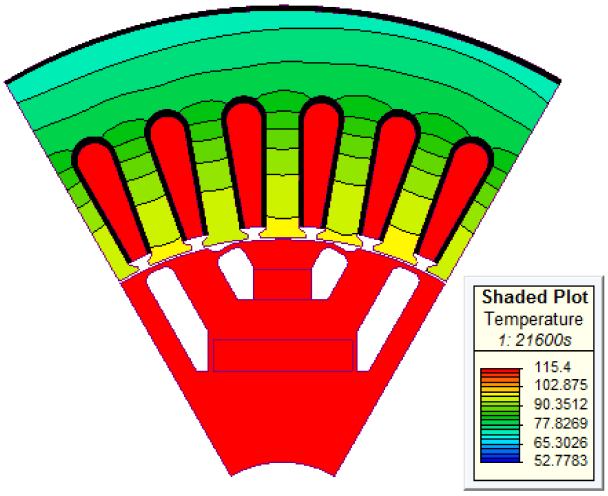

Fig. 7: 2D temperature distribution in the machine with the stator slot lining, impregnation, insulation and imperfection of mechanical fitting accounted for (coolant temperature 50°C).

composite layer was created around the copper winding as shown in the 2D FE model. As explained in section III(A.3), there exists a tiny interface gap between the water-cooled frame and the stator lamination. This was taken into account in the FE analysis by adding an artificial composite layer in the model. These artificial layers are purposely made larger than their true size to avoid creating layers of tiny ill-conditioned triangle elements, which in turn would negatively affect the computational accuracy and converging time. The material properties were then adjusted to ensure the correct contact thermal resistance values. The key thermal properties used in the IPM 2D thermal FE model are given in Table III.

To evaluate the impact of the slot lining, impregnation, insulation and the imperfection of mechanical interface to the temperature distribution inside the IPM machine, both 2D FE thermal models with and without contact resistance layers respectively were constructed and solved.

1) Comparison of results: These results are shown in Figs 6-7. It is evident that the more practical detail the thermal model contains the more realistic the temperature distribution becomes. Although the accuracy of the 2D FE results may be subjected to further experimental verifications, the results obtained from the more detailed 2D FE model show closer correlation to the analytical results. Unlike in analytical model the end-winding copper loss is not included in 2D FE model, which implies the comparison between the two methods is not strictly valid. To form a fair basis for the comparison, the analytical thermal results that exclude the effect of end-winding are also presented in Table V. It can be seen that both results correlate well.

TABLE V: Predicted temperatures of the motor (coolant 50°C)

Machine components	**2D FEM ideal**	**2D FEM with slot liner & frame interface**	**Analytical without end-winding**
Coolant (°C)	50	50	51.3
Frame (°C)	69.8	52.8	52.8
Stator yoke (°C)	73	76	70.2
Stator teeth (°C)	78	89.3	89.8
Main winding (°C)	78	115.2	115.4
Air-gap (°C)	-	-	101.9
Rotor pole (°C)	104.7	113.3	113.9
Top magnets (°C)	106.2	114	114
Middle lamination (°C)	106.9	114.2	114.1
Low magnets (°C)	108.6	114.8	113.9
Rotor yoke (°C)	109.3	114.4	113.5
Shaft (°C)	112	112	112

B. 3D FEM analysis

Fig. 8 shows the 3D FEM model of the IPM machine, which is also 1/6th of the whole machine as only a half stack length is modeled. The water cooling effect is provided by applying an equivalent heat transfer coefficient on the stator outside surface, which is determined analytically. The heat dissipated through the shaft is modeled by adding an artificial thermal resistance that is equivalent to the total thermal resistance of the heat flow path from the shaft to the frame. Unlike ThermNet 2D package, JMAG 3D makes provision for the interface thermal resistances to be included in the thermal calculation by incorporating an analytical thermal equivalent circuit. In addition, JMAG 3D also allows end-winding of the IPM machine to be taken into account. Some important thermal parameters used in the 3D JMAG model are summarized in Table VI.

1) Comparison of the results: Fig. 8 shows the computed 3D temperature distribution inside the IPM machine. As expected, the maximum temperature region is the end-winding. The predicted steady-state temperatures of various components in the machine by 3D FE model are compared with those of LPTM in Table VII. To ensure the same condition as that of the LPTM, a constant temperature boundary was assigned

TABLE VI: Key parameters used in 3D FEM model

Definition	Values
Convective heat transfer coefficient (stator/coolant)	3409 (W/m^2°C)
Convective heat transfer coefficient (stator/rotor)	130 (W/m^2°C)
Thermal contact resistance (shaft/frame)	11.85 (°C/W)
Thermal contact resistance (coil/stator)	0.1986 (°C/W)
Thermal contact resistance (stator/cooling jacket)	0.0849 (°C/W)

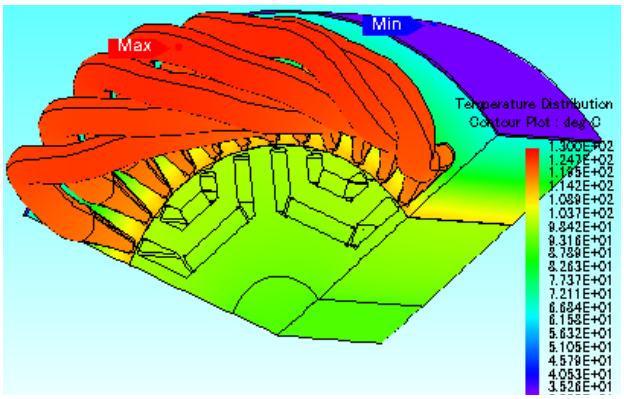

Fig. 8: 3D temperature distribution in the machine from end-winding side (coolant temperature 30°C).

to the shaft surface of the 3D FE model together with a contact thermal resistance. In this way, the heat flows through the shaft for both models are equivalent. The 3D FE results show generally good correlation with those of the LPTM. However, the calculated winding temperatures by LPTM are higher than that of 3D FE, which may be attributed to the radial representation of the heat flow used in LPTM. Since the heat transfer (*convection* and *radiation*) between the stator end-winding and the stator yoke was not included in LPTM, the calculated stator yoke temperature by LPTM shows a lower value than that from 3D FEM.

TABLE VII: Predicted temperature distribution of the IPM machine (coolant 30°C)

Machine components	3D FEM with end-winding	Analytical Quasi-3D
Coolant (°C)	30	31.8
Frame (°C)	34	34.1
Stator yoke (°C)	68.4	58.9
Stator teeth (°C)	91	87.8
Main winding (°C)	115	131.2
End-winding (°C)	127	144.2
Air-gap (°C)	-	98.7
Rotor pole (°C)	111.5	109.6
Top magnets (°C)	112.5	109.7
Middle lamination (°C)	112	109.6
Low magnets (°C)	111	109.3
Rotor yoke (°C)	110.9	108.8
Shaft (°C)	106	106.9
Bearings (°C)	-	47.7
End-shields (°C)	-	40.9
End-space air (°C)	-	87.3

V. Conclusion

A quasi-3D LPTM has been presented for the thermal analysis of a water-cooled IPM machine in this paper. The described analytical model takes into account both the radial heat flow in active section of the machine and the axial heat flow through end-winding region and shaft. To validate the model, the analytical results were compared with those from 2D and 3D FE thermal analysis. The results from LPTM correlate very well with the ones from 2D FE thermal analysis. However, the discrepancy between the LPTM and 3D FE thermal results are relatively large, which is possibly due to the radial heat flow simplification used in the LPTM. The accuracy of the FEM thermal analysis also depends on the heat transfer boundary conditions and contact resistances, which are usually determined by either analytical calculation or empirical formula. It is necessary to conduct thermal measurements to provide a benchmark for these computed results.

Acknowledgment

This work was supported in part by the National Research Foundation (NRF), Eskom Tertiary Education Support Program (TESP) and Stellenbosch University, all of South Africa.

References

[1] B. Funieru and A. Binder, *Thermal design of a permanent magnet motor used for gearless railway traction*, Proc. of 34th Annual Conf. of IEEE Industrial Electronics Society (IECON), pp. 2061-2066, 2008.

[2] J. Fan, C. Zhang, Z.Wang, Y. Dong, C.E. Nino, A.R. Tariq, and E.G. Strangas, *Thermal analysis of permanent magnet motor for the electric vehicle application considering driving duty cycle*, IEEE T-MAG 46(6):2493-2496, 2010.

[3] A. M. EL-Refaie, N. C. Harris, T. M. Jahns and K. M. Rahman, *Thermal analysis of multibarrier interior PM synchronous machine using lumped parameter model*, IEEE T-EC 19(2):303-309, 2004.

[4] W. Tong, S. Wu, Z. An, and R. Tang, *Thermal analysis of direct-drive permanent magnet wind generator using both lumped larameter network and finite element method*, Asia-Pacific Power and Energy Engineering Conference (APPEEC), pp. 1-4, 2010.

[5] D. Joo, J. Cho, K. Woo, B. Kim, D. Kim, *Electromagnetic field and thermal linked analysis of interior permanent-magnet synchronous motor for agricultural electric vehicle*, IEEE T-MAG 47(10):4242-4245, 2011.

[6] JMAG Designer 11.1-JMAG Designer OnlineHelp.

[7] H. Polinder, M.J. Hoeijmakers, *Eddy Current Losses in the permanent magnets of a PM machine*, IEE-EMD Conference Record, 1-3 Sept, 1997.

[8] J.F. Gieras and M. Wing, *Permanent Magnet Motor Technology - Design and Applications*, Marcel Dekker, New York, 2002.

[9] S. Nategh, O. Wallmark, M. Leksell, *Thermal analysis of permanent-magnet synchronous reluctance machines*, Proc. of the 14th European Conf. on Power Electronics and Applications (EPE), pp.1-10, 2011.

[10] J. Fan, C. Zhang, Z. Wang, et al, *Thermal analysis of permanent magnet motor for the electric vehicle application considering driving duty cycle*, IEEE T-MAG 46(6):2493-2496, 2010.

[11] G. Kylander, *Thermal modelling of small cage-induction motors*, PhD dissertation, Chalmers University of Technology, Sweden, 1995.

[12] J. Holman, *Heat Transfer*, McGraw-Hill, London, 1992.

[13] S. Nategh, O. Wallmark, M. Leksell, S. Zhao, *Thermal analysis of PMaSRM using partial FEA and lumped parameter modeling*, IEEE T-EC 27(2):477-488, 2012.

[14] D. P. Kulkarni, G. Rupertus and E. Chen, *Experimental investigation of contact resistance for water cooled jacket for electric motors and generators*, IEEE T-EC 27(1):204-210, 2012.

[15] J. Lindström, *Thermal Model of a Permanent-Magnet Motor for a Hybrid Electric Vehicle*, Research Report, Dept. of Electric Power Engineering, Chalmers University of Technology, Goteborg, Sweden, 1999.